PAPER

Check for updates

Catalytic effects of iron adatoms in poly(*para*-phenylene) synthesis on rutile TiO₂(110)†

Mohammadreza Rostami,[a] Biao Yang, [ID] *[a,b] Xiaochuan Ma,[c] Sifan You, [ID] [b] Jin Zhou, [ID] [c] Meng Zhang,[b] Xuefeng Cui,[c] Haiming Zhang, [ID] [b] Francesco Allegretti, [ID] [a] Bing Wang, [ID] *[c] Lifeng Chi [ID] *[b] and Johannes V. Barth*[a]

n-Armchair graphene nanoribbons (nAGNRs) are promising components for next-generation nanoelectronics due to their controllable band gap, which depends on their width and edge structure. Using non-metal surfaces for fabricating nAGNRs gives access to reliable information on their electronic properties. We investigated the influence of light and iron adatoms on the debromination of 4,4′′-dibromo-*p*-terphenyl precursors affording poly(*para*-phenylene) (PPP as the narrowest GNR) wires through the Ullmann coupling reaction on a rutile TiO₂(110) surface, which we studied by scanning tunneling microscopy and X-ray photoemission spectroscopy. The temperature threshold for bromine bond cleavage and desorption is reduced upon exposure to UV light (240−395 nm wavelength), but the reaction yield could not be improved. However, in the presence of codeposited iron adatoms, precursor debromination occurred even at 77 K, allowing for Ullmann coupling and PPP wire formation at 300−400 K, *i.e.*, markedly lower temperatures compared to the conditions without iron adatoms. Furthermore, scanning tunneling spectroscopy data reveal that adsorbed PPP wires feature a band gap of ≈3.1 eV.

Introduction

Ullmann coupling, a widely employed, controllable reaction for on-surface synthesis, is a versatile tool for fabricating surface-confined low-dimensional molecular nanostructures.[1,2] Ullmann coupling is a simple, predictive, and efficient on-surface reaction,[3,4] typically involving two main steps: the dehalogenation of molecules and the coupling of the resulting radicals to generate a desired product.[1,2] Often the metal substrate initiates dehalogenation reactions,[2] whereby the abstracted halogen atoms resulting from the dissociation of carbon–halogen (C–X) bonds remain chemisorbed at the substrate.[5,6] This widespread mechanism enables the direct bonding of aromatics and the synthesis of π-conjugated structures. Selective and directional nanoarchitecture can be achieved by using different halogen substituents and molecular moieties, exploiting the associated specific C–X bond dissociation energies. This promising control of on-surface reaction paves the way for designing complex nanoarchitectures and molecular electronics.[7] Many custom-designed precursors have been reported[8] for the fabrication of 0D, 1D and 2D covalent nanostructures, such as cyclic structures, linear or zigzag wires and ribbons, and 2D porous or dense networks[2] with extended regularity and long-range order through Ullmann coupling reactions. These include mostly brominated[1,2,7,9,10] and iodinated compounds.[2,7,11]

Poly(*para*-phenylene) (PPP) wires, which represent the narrowest *n*-armchair graphene nanoribbons (nAGNRs) (*n* = 3) are large band gap semiconductors.[12] The parameter "*n*" refers to the number of carbon atoms defining the width of an nAGNR.[5] PPP wires feature great potential for next-generation electronics due to their promising mechanical properties, high stability, low density, and tunable band gap controlled by doping.[12,13] nAGNRs are typically formed *via* the polymerization of precursors containing bromine (Br),[5,13–15] such as 4,4′′-dibromo-*p*-terphenyl (DBTP),[16–18] or iodine.[15] The on-surface synthesis strategy offers a promising route to the successful preparation of nAGNRs, but unfortunately the typically applied metal surfaces limit the further study and application due to the quenching of electronic and optical excitations.[12] Thus, non-metal substrates, with well-defined surface structures and interactions, need to be explored for further studies

[a]*Physics Department E20, School of Natural Sciences, Technical University of Munich, Garching, 85748, Germany. E-mail: jvb@tum.de*
[b]*Institute of Functional Nano & Soft Materials (FUNSOM), Joint International Research Laboratory of Carbon-Based Functional Materials and Devices, Soochow University, Suzhou, 215123, P. R. China. E-mail: chilf@suda.edu.cn, yangbiao@suda.edu.cn*
[c]*Hefei National Research Center for Physical Sciences at the Microscale and Synergetic Innovation Center of Quantum Information & Quantum Physics, New Cornerstone Science Laboratory, University of Science and Technology of China, Hefei, 230026, China*
†Electronic supplementary information (ESI) available. See DOI: https://doi.org/10.1039/d4nr04407j

of nAGNRs.[5] Utilizing such alternative substrates[14,19–21] including semiconductors[1,2,9,13,22–26] or insulating oxides,[27–31] results in more reliable information about the electronic properties of nAGNRs.[26,32–38]

Notably titanium dioxide (TiO_2) surfaces, as semiconducting oxide surfaces like rutile (011),[39–41] rutile (110),[42–48] and anatase (101),[49–55] are promising substrates for surface-assisted reactions, preventing electrons transfer between the on-surface structures and the substrate.[40,56] The most energetically favourable and stable TiO_2 crystalline surface is rutile (110).[40,47,57–61] Rutile is commonly synthesized in laboratories, reducing its price and promoting its applications.[40,50] Although the absence of catalytically active metal substrates/adatoms and metal–organic intermediates reduces the efficiency of on-surface Ullmann coupling,[4,39] UV light can induce debromination of precursors, followed by Ullmann coupling and GNR formation, as confirmed by corresponding density functional theory (DFT) calculations and experiments.[2,57,62–67] Additionally, the lower conductivity of semiconducting TiO_2 crystals compared to metals may hinder the implementation of surface science techniques, such as X-ray photoelectron spectroscopy (XPS), scanning tunnelling microscopy (STM), and low-energy electron diffraction (LEED).[46] Therefore, shrinking the rutile TiO_2 band gaps through reducing the crystal due to the creation of crystallographic shears, O vacancies, and anti-phase domains by repeated cycles of sputtering and annealing facilitates their application as substrates.[40,46,47,68,69] Annealing at temperatures lower than ≈973 K affords a clean surface with distinct LEED pattern.[45] Annealing at temperatures exceeding ≈973 K without O dosing results in the formation of (1 × 2) defects aligned along the ⟨1$\bar{1}$0⟩ direction.[45] Annealing at temperatures above 1200 K causes unwanted surface faceting and corrugating.[45]

Debromination and Ullmann coupling of DBTP molecules[44] and 10,10″-dibromo-1′,4′-difluoro-9,9′:10′,9″-teranthracene,[41] leading to the formation of PPP wires,[44] and 7AGNRs[41,70] on rutile $TiO_2(110)$[71] and (011), respectively, have been reported. Moreover, recent findings report Ullmann coupling of DBTP and diiodo-terphenyl on TiO_2 boosted by the addition of cobalt adatoms, as demonstrated through XPS and angle-resolved photoelectron spectroscopy (ARPES).[4] However, further and more detailed STM studies on the catalytic effects induced by different metallic adatoms and light irradiation on the on-surface synthesis of PPP wires are lacking. In this work, we investigated both iron (Fe) adatom and photo-catalytic effects[12] on the debromination of DBTP molecules, the subsequent Ullmann coupling on rutile TiO_2, and the desorption of the resulting Br atoms using STM and XPS. Moreover, the band gap of the prepared PPP wires could be determined using scanning tunnelling spectroscopy (STS).

Results and discussion

The rutile $TiO_2(110)$ surface was prepared by repeated cycles of sputtering and annealing at approximately 900 K. Fig. 1a shows a LEED pattern of rutile $TiO_2(110)$ surface, indicating a (1 × 1) atomic lattice without interfering charging effects, i.e., there is an unperturbed clean surface, in agreement with the literature.[40,72] Fig. 1b depicts corresponding large-scale STM data, displaying terraces of various sizes. The STM imaging is primarily influenced by the density of states rather than morphological features.[40] The Ti and O rows manifest as bright and dark lines, respectively, with an inter-row distance of approximately 6.5 Å, consistent with the reported unit cell lattice parameter.[40] The formation of some TiO_2 clusters and (1 × 2) defects (missing O rows, purple arrow in Fig. 1b) was also observed. Heating the rutile $TiO_2(110)$ surface to approximately 973 K without O_2 treatment resulted in the formation of a (1 × 2) superstructure and likely TiO_2 strings oriented parallel to O and Ti rows ([001]).[41,45,73–78] The zoom-in STM image in Fig. 1c shows some TiO_2 clusters (marked by pink arrows) centered on the Ti rows and hydroxyls (yellow arrow) at the O rows. The most abundant surface donors, O vacancies, appear as bright bridges spanning the dark stripes of the O rows, connecting the bright O atom rows on the TiO_2 surface.[69] Fig. 1d shows an STM image of a DBTP submonolayer on rutile $TiO_2(110)$ deposited at room temperature. Single, unreacted DBTP molecules (blue arrow) are mostly adsorbed on the Ti rows, similar to isolated Br atoms (red arrow) abstracted from DBTP. Hydroxyls (yellow arrow) located on O rows appear as smaller and darker spheres compared to the Br atoms in the STM image. In addition, the green arrow indicates an O vacancy in this region. Fig. 1e shows a zoom-in STM image of a densely packed DBTP cluster, indicating the coexistence of a longer unreacted DBTP (≈1.9 nm, blue arrow, with the Br indicated by a red arrow) and an adjacent shorter debrominated DBTP species (≈1.6 nm, white arrow), reflecting some degree of on-surface debromination at 300 K. Fig. 1f presents structure models of the resulting rutile $TiO_2(110)$ surface,[79] including key features such as a bridging hydroxyl (yellow arrow),[80] a surface-bonded Br atom (red arrow), an O vacancy (green arrow), and both unreacted (blue arrow) and debrominated (white arrow) DBTP molecules (Fig. S1†).

Fig. 2a illustrates a DBTP submonolayer after annealing a 300 K-deposited DBTP monolayer (ML) at 400 K. Ullmann coupling and the formation of DBTP dimers on the Ti substrate rows are clearly observed, as indicated by blue arrows. The presence of Br adatoms and hydroxyl species is also inferred. Upon annealing at 500 K, PPP short wires formed and prevailed on the surface, as seen in Fig. 2b, running parallel to the O and Ti rows, centered on the Ti rows (still coexisting with Br adatoms and hydroxyl compounds). Two types of PPP wires exist: one group appears thinner and darker with an asymmetrical shape and charge distribution, and the other type, observed sparsely, appears wider and brighter with a symmetrical shape. As indicated in the STM image in Fig. 2c by yellow and blue arrows, we interpret the asymmetrical wires in terms of tilted PPP wires, as previously reported on rutile TiO_2,[44] and the symmetrical ones as flat (less tilted) PPP wires, similar to those reported on metallic surfaces, respectively.[16–18] Schematic atomic models of these two different wire conformations are shown in Fig. 2d.
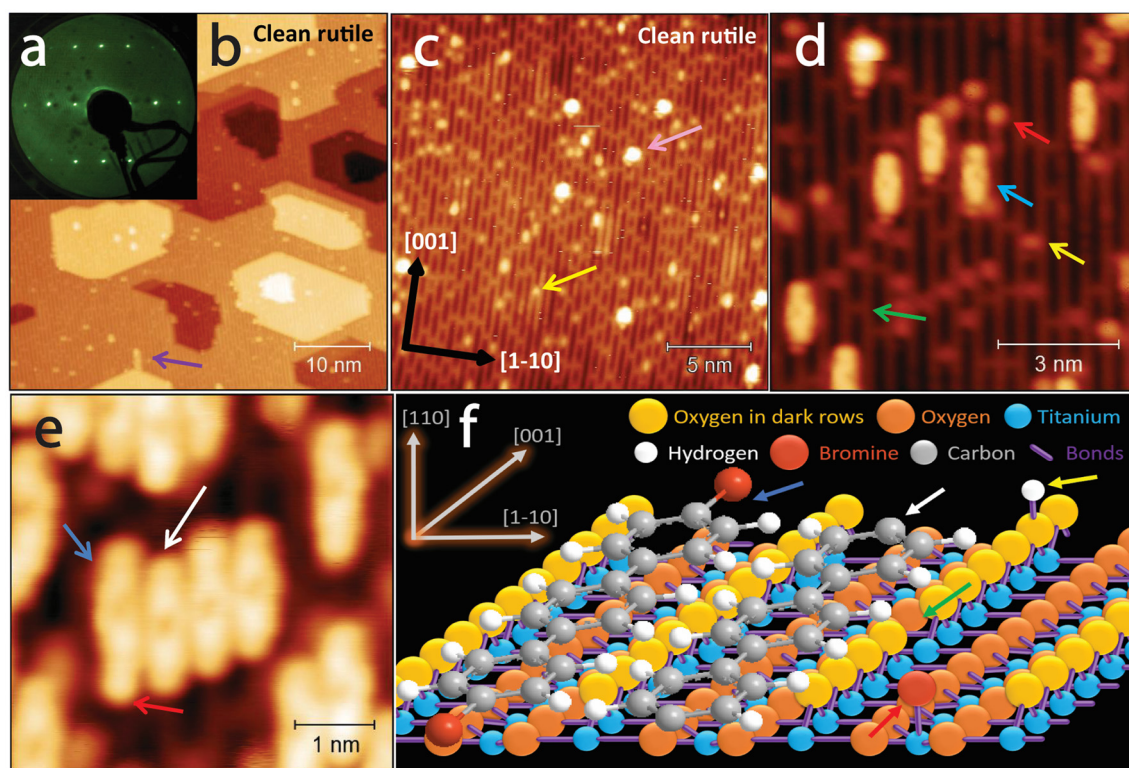
Fig. 1 (a) A (1 × 1) LEED pattern (primary energy: E_{LEED} = 109 eV) and (b, c) STM images of a clean rutile TiO$_2$(110) surface; the distance between the brightest and the darkest point in the STM image corresponds to z-range = 1.25 nm in (b) and z-range = 0.18 nm in (c). The pink and yellow arrows highlight a TiO$_2$ cluster and a hydroxyl, respectively. (d and e) Zoom-in STM images of a DBTP sub-monolayer amount on the rutile TiO$_2$(110) surface with z-range = 0.27 nm (d) and z-range = 0.19 nm (e). In (d), red, blue, yellow, and green arrows denote a Br atom, a DBTP molecule, a hydroxyl, and an O vacancy, respectively. In (e) blue, white, and red arrows indicate a DBTP molecule, a debrominated DBTP molecule, and a Br atom in the DBTP molecule, respectively. (f) Schematic atomic models of the rutile TiO$_2$(110) surface, highlighting key features such as a bridging hydroxyl (yellow arrow), a surface-bonded Br atom (red arrow), an O vacancy (green arrow), an integral DBTP (blue arrow), and a debrominated DBTP (white arrow). The colour scheme for the atomic species is as follows: bridging O atoms in dark rows in the STM images (yellow spheres), subsurface O atoms (orange spheres), titanium atoms (blue spheres), C atoms (gray spheres), hydrogen atoms (white spheres), and Br atoms (red spheres). The surface covalent bonds are represented by purple cylinders. STM acquisition temperature: 77 K, tunnelling parameters: V_s = −1 V, I_t = 10 pA.

Additionally, upon annealing at 600 K, most Br atoms and hydroxyl compounds desorbed from the substrate (see Fig. 2c). Moreover, some ribbons shifted from their primary stable orientations to different orientations, such as a bent conformation extending at an angle of nearly 45° relative to the ⟨1̄10⟩ substrate direction. The appearance of shorter wires and more clusters indicates the onset of PPP wire dissociation. Upon annealing at 700 K, we ensured the complete desorption of Br atoms and hydroxyls (see STM image in Fig. 2e), whereby on the flip side, PPP wires were frequently dissociated, and the density of molecular clusters exceeds that of wires or ribbons (Fig. S2–S4†).

This process was further characterized chemically by XPS. The data in Fig. 2f, reveal, after deposition at liquid nitrogen (LN$_2$) temperature (77 K), a Br 3d signature with broad peak due to spin–orbit coupling.[16–18] By annealing at higher temperatures, as debromination increasingly occurs, the distinct shoulder at lower binding energies, related to separated Br atoms, is enhanced. In addition, with the formation of covalent chains, the C 1s XPS peak shifts to lower binding energies (Fig. S5†). At approximately 500 K, the C–Br component vanishes and Ti–Br counterpart dominates the Br 3d XP spectrum, in agreement with STM observations. Br desorption was also observed upon increasing the annealing temperature, which could be completed by further increasing the temperature and time.

Leveraging light for on-surface reactions and polymerizations holds significant promise for promoting Ullmann coupling at reduced temperatures and on less reactive surfaces as compared to thermal activation.[62] Photo-induced coupling can improve the control of on-surface reactions through the precise adjustment of photon intensity and wavelength. Photons with specific energies can selectively break various covalent bonds. Therefore, we studied the effect of illuminating the surface with a Xe lamp filtered to deliver wavelengths in the UV range (240–395 nm). However, irradiation with Xe light did not change the onset temperature or the density of PPP evolution significantly; instead, the desorption of separated Br atoms from the surface was favored by illumination. Fig. 3a and b depict PPP wires after annealing at 500 K without
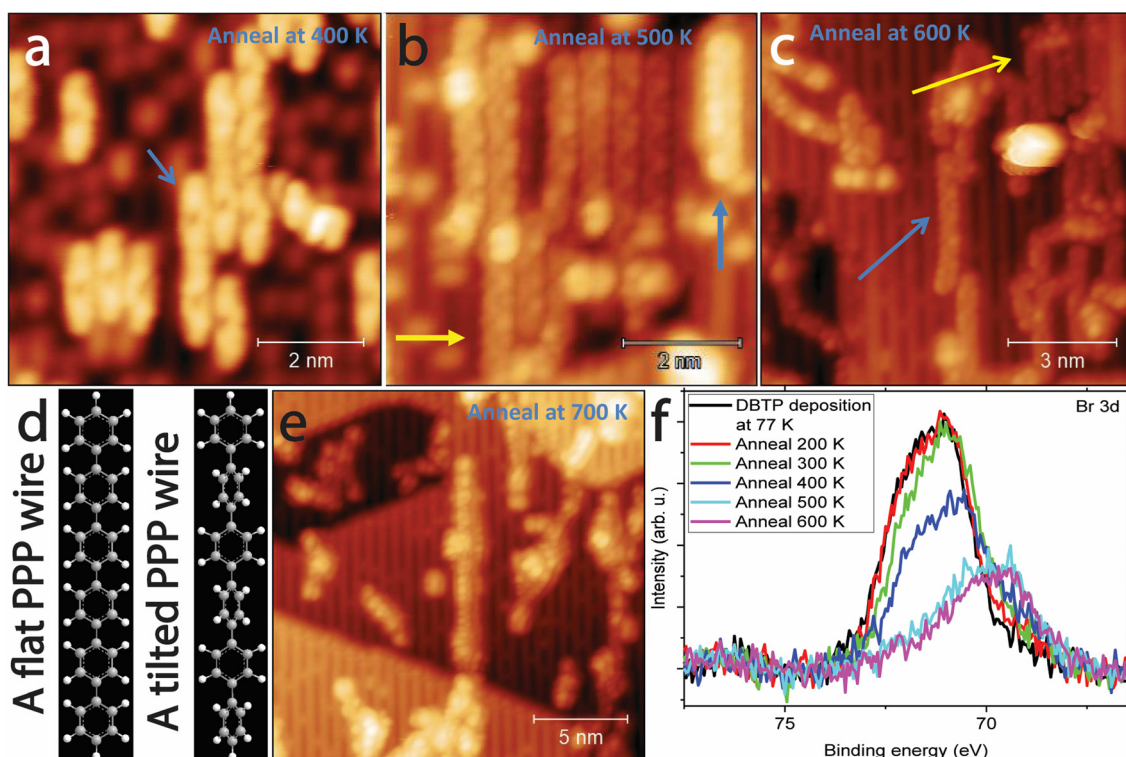
Fig. 2 (a) STM image of a DBTP sub-monolayer coverage on a rutile TiO$_2$(110) surface after annealing a DBTP ML at 400 K (z-range = 0.22 nm). The blue arrow denotes a DBTP dimer after Ullmann coupling. STM images of PPP wires on the rutile TiO$_2$(110) surface after annealing at (b) 500 K (z-range = 0.45 nm) and (c) 600 K (z-range = 0.68 nm). Yellow and blue arrows mark tilted ($\approx$0.4 nm) and flat ($\approx$0.6 nm) conformation of adsorbed PPP wires, respectively. Br atoms were desorbed at 600 K and the rutile TiO$_2$ surface appears cleaner. (d) Schematic atomic models of a flat (left) and a tilted (right) PPP wire made in ChemDraw software. Gray and white spheres represent C and H atoms, respectively. (e) STM image of the sample after annealing at 700 K, showing the dissociation of PPP (z-range = 0.78 nm). (f) Br 3d narrow region scan XPS spectra of a rutile TiO$_2$(110) surface after deposition of a DBTP ML at 77 K and annealing it at different temperatures. All STM and XPS data were acquired at 77 K. STM tunneling parameters: V_s = −1 V, I_t = 10 pA.
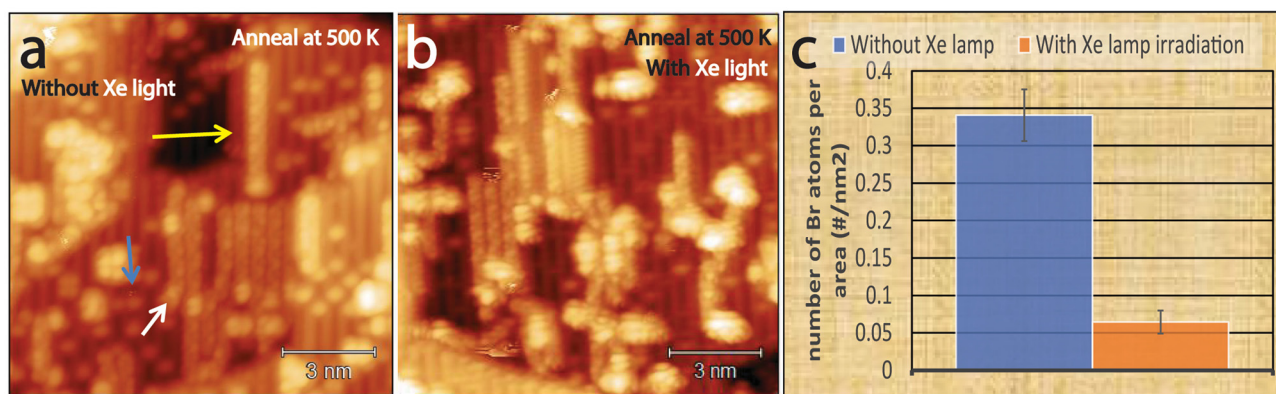

Fig. 3 (a) STM image of PPP wires on a rutile TiO$_2$(110) surface after annealing at 500 K without Xe lamp irradiation; z-range = 0.77 nm. Yellow, white, and blue arrows indicate PPP wires with flat conformation, PPP wires with tilted conformation, and a bromine atom, respectively. (b) STM image of PPP wires on the rutile TiO$_2$(110) surface after annealing at 500 K in the presence of a Xe lamp irradiation (wavelengths: 240−395 nm); z-range = 0.54 nm. (c) Histogram of the average number of bromine atoms per nm^2 as detected on the surface with (orange) and without (blue) the Xe lamp irradiation. STM acquisition temperature: 77 K. STM tunneling parameters: V_s = −1 V, I_t = 10 pA.

and with irradiating by the Xe lamp (during cooling from the final annealing temperature to room temperature), respectively. Yellow, white, and blue arrows indicate a PPP wire with a

flat conformation, a PPP wire with a tilted conformation, and a separated Br atom, respectively. At first glance, the surface exposed to irradiation appears cleaner, with fewer Br atoms

compared to the surface without irradiation. Fig. 3c compares the Br surface density with and without irradiation. For each case, four different STM images were analyzed, the Br atoms were counted, normalized by area, and the average values were calculated and plotted in this histogram. As illustrated, an average of 0.34 and 0.06 Br atoms per nm^2 was measured on the surface without and with irradiation of a DBTP multilayer (≈ 3 ML), respectively. Consequently, these measurements confirm photo-stimulated desorption of Br atoms after debromination of DBTP, and the formation of PPP wires upon annealing at 500 K.

While light enhances the cleavage of Br bonds on the surface and possibly within the molecules, the length of the PPP wires remains limited to below 10 nm. Thus, the efficiency of PPP formation is limited, presumably due to the absence of the metal adatoms needed for the chain formation of metal–organic intermediates. These reaction intermediates are frequently encountered as the second step of the Ullmann coupling on metallic surfaces before C–C coupling.[16–18] Therefore, we investigated the influence of codeposited Fe adatoms as catalysts. Fig. 4a shows the surface of rutile $TiO_2(110)$ after deposition of a DBTP ML and annealing at
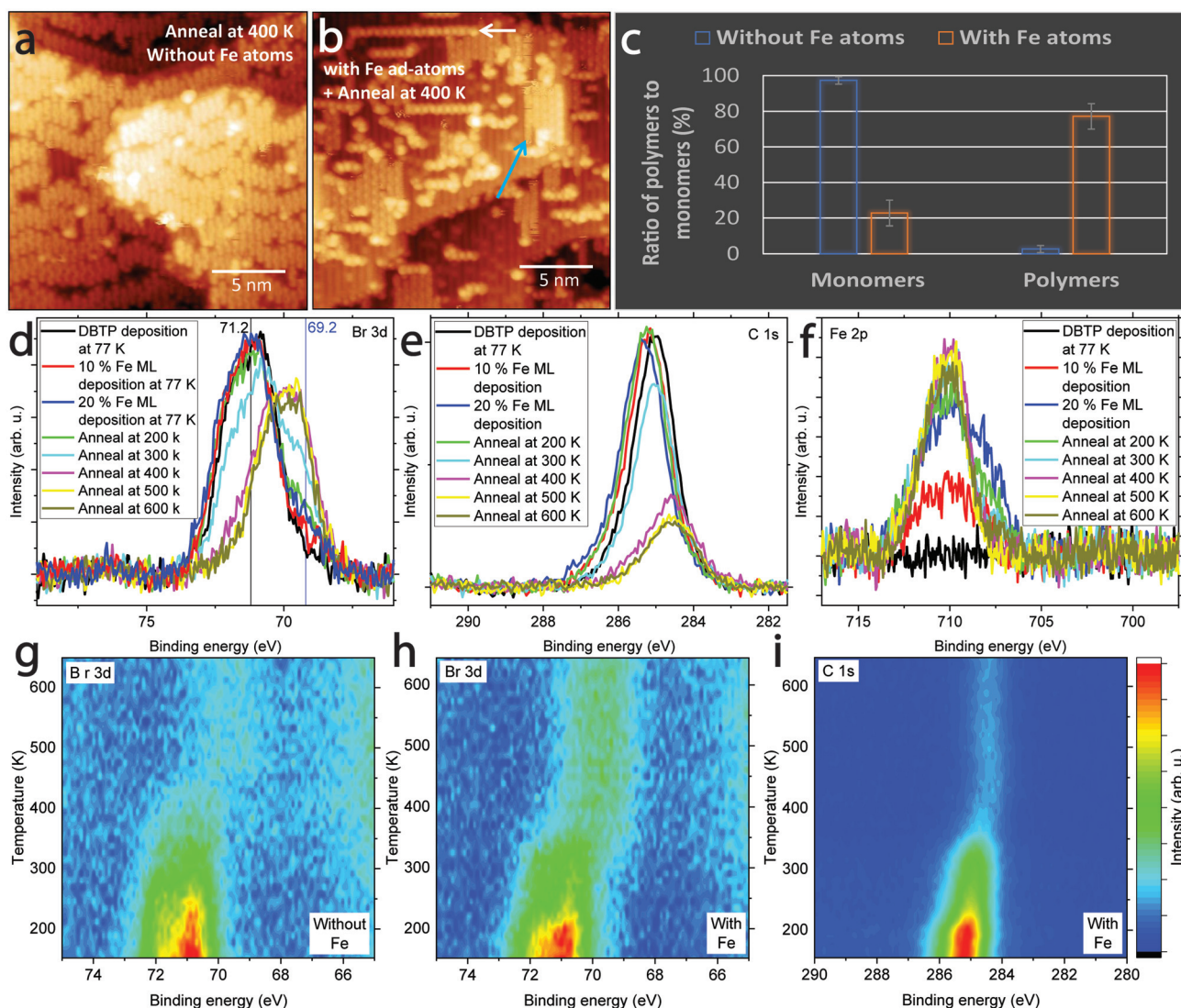

Fig. 4 (a) STM image of a DBTP ML on a rutile $TiO_2(110)$ surface after annealing at 400 K (30 minutes); z-range = 0.62 nm. (b) STM image of PPP wires on rutile $TiO_2(110)$ after DBTP molecule and Fe atom deposition (estimated coverage of 0.1 ML) on this surface and annealing at 400 K (30 minutes); z-range = 0.84 nm. White and blue arrows indicate the Fe adatoms and PPP wires, respectively. (c) Histogram of the average number of the monomers and polymers observed on the surface with and without Fe atoms. (d) Br 3d, (e) C 1s, and (f) Fe 2p narrow region XP spectra of a rutile $TiO_2(110)$ surface after deposition of a DBTP ML and subsequently an Fe sub-monolayer (coverages of 10% and 20%) at 77 K and annealing the sample at different temperatures. (g) TP-XPS of the zoomed-in Br 3d core level region after deposition of DBTP molecules on the surface. TP-XPS of the zoomed-in (h) Br 3d and (i) C 1s core level regions after deposition of DBTP molecules and Fe ad-atoms on the surface. XPS and STM acquisition temperature: 77 K. STM tunneling parameters: $V_s = -1$ V, $I_t = 10$ pA.

400 K, whereupon most of the molecules are single without any polymerization. Fig. 4b depicts an STM image after deposition of 0.1 ML coverage of Fe atoms at temperatures below 273 K and a DBTP ML using the same parameters as in Fig. 4a, followed by annealing at 400 K. The Fe atoms (white arrow) primarily assembled in lines perpendicular to the O and Ti rows. The formation of organometallic chains of debrominated DBTP and Fe atoms was both expected[4] and observed. Ullmann coupling was catalyzed by Fe adatoms, resulting in PPP wires (blue arrow) becoming dominant, mostly appearing around Fe adatoms, although Fe does not remain in the polymer chains. To confirm these results quantitatively, we analyzed four STM images of the surface and DBTP ML deposition after annealing at 400 K without Fe adatoms and four STM images with a precoverage of 0.1 ML Fe. In each case, the ratio of the DBTP monomers to polymers was counted, normalized by the area, and the average values were calculated and plotted in the histogram shown in Fig. 4c. As illustrated, for pure DBTP ML deposition and annealing, only ≈3% of adsorbed DBTP undergo a coupling reaction at 400 K. On the other hand, in the presence 0.1 ML Fe using the same procedure, about 77% of the DBTP compounds covalently connected at the same temperature, and merely ≈23% remaining in form of monomers. This finding thus supports the conclusion that Fe adatoms catalyze and enhance Ullmann coupling and the formation of PPP wires at reduced temperatures (Fig. S4†).

Further XPS investigations were conducted to provide additional evidence and insight into this catalytic effect. After deposition a DBTP ML at LN_2 temperature on the rutile $TiO_2(110)$ surface, 0.1 ML of Fe atoms were initially deposited, followed by an additional 0.1 ML (totaling 0.2 ML). Somewhat surprisingly, Fig. 4d shows an increase in the Br 3d shoulder for Br atoms detached from DBTP molecules and bonded to the surface and likely to the Fe adatoms at 77 K, in contrast to Fig. 2f. Therefore, the debromination reaction was initiated even at LN_2 temperature in the presence of Fe adatoms, demonstrating the remarkable catalytic effect of these metallic adatoms entailing PPP wire formation. Conversely, upon higher temperature annealing, more complex Br atoms remain on the surface, pointing to strong bonds between Fe and Br that prevent Br desorption at lower temperatures. In addition, the C 1s core level XPS spectra in Fig. 4e also show different behavior in the presence of Fe adatoms. After Fe deposition on a DBTP ML, the C 1s core level peak initially shifts to higher binding energies and upon annealing at higher temperatures, to lower binding energies due to debromination and C–C coupling, whereby significant C desorption occurred, which is consistent with the STM results. Fig. 4f presents the XPS spectra of Fe 2p core level electrons on this surface. After deposition at 77 K, the Fe 2p peak is broadened, presumably due to the presence of various bonds involving Fe on the surface, such as Fe–O (≈710–711 eV),[81,82] Fe–Br (≈710–711 eV),[83,84] Fe–C (≈707–708 eV),[85–87] and Fe–Fe (≈707 eV).[88] Upon annealing, interestingly, we find a reduced full width at half maximum (FWHM), and a peak shift to higher binding energies, characteristic of Fe–halogen bonds, indicating that Fe–Br atoms clus-
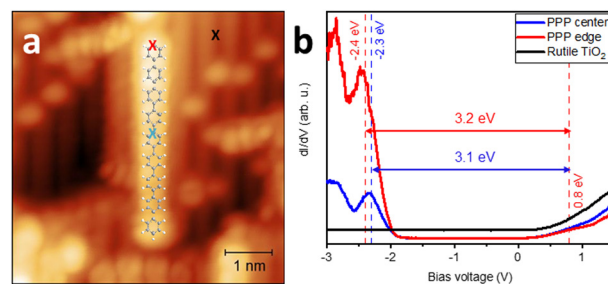

Fig. 5 (a) STM image with proposed atomic model of a flat PPP wire on rutile TiO_2 after annealing a DBTP ML at 500 K; z-range = 0.51 nm, V_s = −1 V, I_t = 10 pA. (b) Tunneling spectra of the spots shown in (a). STM/STS data acquisition at T = 77 K.

ters accumulate on the surface. Moreover, spectra by temperature-programmed XPS (TP-XPS) show that in the absence of Fe adatoms a significant debromination shift for both Br 3d (Fig. 4g) and C 1s (Fig. S5†) core level regions occurs at ≈450 K (thus clearly above the 400 K used otherwise). In contrast, the dominant debromination shift for both the Br 3d (Fig. 4h) and C 1s (Fig. 4i) core levels in the presence of Fe ad-atoms starts already at 350 K. Consequently, Ullmann coupling and formation of 3AGNRs (PPP wires) are consistently catalyzed by Fe adatoms.

Finally, Fig. 5a shows a flat adsorbed PPP wire along with the proposed, optimized atomic structural model. The PPP shape and extension suggests that it results from the Ullmann coupling of three DBTP units. Red, blue, and black crosses denote the PPP edge and center, and rutile surface, respectively, where STS studies were conducted and plotted in Fig. 5b. The corresponding black curve depicts spectra of a clean rutile TiO_2 surface, where the conduction band (CB) onset is located at a bias voltage of ≈0.3 V and the valence band (VB) appears at a bias voltage of approximately −3 V (Fig. S1g†).[89–93] The overlap of the CB states with the PPP lowest unoccupied molecular orbital (LUMO) complicates their identification, yet the latter is visible as a shoulder at ≈+0.8 V. Since the STS curves of rutile TiO_2 are flatter for negative bias, the highest occupied molecular orbital (HOMO) appears more pronounced in this region, peaking at −2.3 V and −2.4 V for the PPP center and edge, respectively. Thus, a band gap value of ≈3.1 can be assigned to the PPP, confirming wide-band gap semiconducting behavior. The band gap values of ≈3.3 eV,[94] ≈3.2 eV,[95] and ≈3.0 eV (ref. 96) for PPP on Au (111) and ≈1.1 eV (ref. 97) on Cu (110) were reported in the literature. In addition, this demonstrates the decoupling effect of the surface, preventing the quenching of the electronic excitation of the fabricated GNRs, which is required for precise measurements of the electronic and optical properties of the on-surface nanoarchitectures.

Conclusions

In conclusion, we have investigated the behaviour of DBTP submonolayers, MLs, and multilayers on atomically well-

defined rutile $TiO_2(110)$. The debromination of DBTP molecules sets in at 200 K, and the desorption of the Br atoms abstracted from the molecules becomes appreciable for temperatures above 400 K. After annealing at 400 K, sparse DBTP dimers evolve through on-surface Ullmann coupling. Upon further annealing at 500 K, PPP wires prevail on the surface, undergoing dissociation reactions for $T \geq 700$ K. Upon irradiating the surface with UV light (wavelength range 240–395 nm), Br-substrate and Br–C molecular bonds were cleaved at lower annealing temperatures, entailing desorption of most Br at a reduced temperature of ≈500 K, thus yielding a cleaner surface following PPP wire formation. Furthermore, the deliberate deposition of Fe adatoms exerts a remarkable catalytic effect on the Ullmann coupling reaction. Thus, with small doses of these metal adatoms partial debromination of DBTP occurs even at LN_2 temperature (77 K). This significant influence of Fe codeposited with DBTP entails a dominance of PPP wires upon annealing at 400 K, while under the same conditions but without Fe adatoms, molecular monomers prevail. Fe atoms and debrominated DBTP at 77 K reduced the activation temperature required for aryl–aryl coupling to 300–400 K. On the other hand, upon higher temperature annealing, more Br atoms bind to Fe atoms on the surface, accumulating in unwanted clusters accounting for a rougher surface with the length of PPP wires limited to below 10 nm. This general feature is ascribed to weaker molecule–surface interactions as compared to metals, causing partial molecular desorption prior to coupling reactions. Furthermore, the reduced rutile substrate exhibits a semiconducting behaviour, favouring the electronic and optical measurements of PPP wires. This property hinders the hybridization and charge transfer between the prepared wires and the substrate, making it suitable for more elaborate studies of the excitation of the on-surface nanostructures. STS results indicate PPP with a wide band gap, holding significant promise for next-generation electronics or other applications.

Experimental

Sample preparation

High-purity single crystals of rutile $TiO_2(110)$ (10 mm × 5 mm) were purchased from Princeton Scientific Corporation, Pennsylvania, USA, and MaTecK, Jülich, Germany, respectively. O vacancies were engineered into these substrates through an extensive 8-hour process of argon ion (Ar^+) sputtering (≈2 keV, 10 minutes, $I_{ion} \approx 24$ μA) followed by annealing (≈900 K, 10 minutes). This treatment enhanced the substrate conductivity, enabling the application of surface science techniques such as XPS, STM, and LEED. The treated TiO_2 crystals changed from transparent to a dark bluish colour. Notably, the rutile TiO_2 surface emitted blue luminescence during sputtering and turned dark reddish upon annealing. Iterative sputtering and annealing cycles yielded atomically flat surfaces.

Characterization

Comprehensive characterization of the rutile $TiO_2(110)$ and molecular samples was performed using XPS (Mg $K_\alpha \approx 1253.6$ eV), TP-XPS, LEED, STS, and STM, following meticulous cleaning in various UHV chambers. In the custom-built XPS chamber at the Technical University of Munich (TUM), a K-type (Nickel–Chromium/Nickel–Aluminum) thermocouple was affixed between molybdenum stripes attached to the TiO_2 surfaces and secured by screws to a molybdenum plate supporting the TiO_2 samples. The chamber maintained a base pressure below 2×10^{-10} mbar, and XPS and LEED measurements were conducted at liquid nitrogen temperature (77 K). In the Omicron STM chamber at the University of Science and Technology of China (USTC), a constant current was applied via a tantalum (Ta) plate directly attached to the rutile TiO_2 underside of the sample. This setup allowed specific voltage applications, inducing resistance changes $\left(R = \dfrac{V}{I} \right)$ and enabling precise sample temperature control according to a parabolic resistance-temperature relationship (Fig. S1†). The preparation and principal STM chambers maintained base pressures below 4.0×10^{-10} mbar and 8.0×10^{-11} mbar, respectively. STM and STS measurements were performed at 77 K using a digital lock-in amplifier with a set point of 1.0 V, 10 pA, an oscillation frequency of 973 Hz, and an amplitude of 10–20 meV.

Molecular deposition

The DBTP molecules were obtained from Shanghai Aladdin Bio-Chem Technology and loaded into quartz crucibles of custom-built molecular organic beam evaporators (OMBEs) for deposition onto pristine TiO_2 (110) surfaces at controlled temperatures (300 K and 77 K). STM and STS characterization of the deposited films revealed insights into thermally- and photo-induced molecular assemblies. Sample heating was achieved through a combination of radiative heating and electron bombardment from a W filament in the XPS chamber, and by passing a constant current through a Ta plate in the STM chamber. In both the STM and XPS chambers, custom-built Fe evaporators facilitated the deposition of approximately 0.1–0.2 ML of Fe atoms at temperatures below 273 K to investigate the catalytic effects of adatoms on the formation of 3AGNRs on these surfaces. The CB and VB states of the rutile $TiO_2(110)$ surface as well as the HOMO and LUMO of the synthesized PPP wires, and the resulting band gaps of both, were characterized via STS. Furthermore, surface irradiation in the STM chamber was ensured by a Xe lamp from Hamamatsu Photonics K. K. (C7535), with a round color filter (FGUV5) from Thorlabs filtering wavelengths below 240 nm and above 395 nm. A filtered Xe lamp beam with a size of about 20 mm × 25 mm and a power of 250 mW reached the sample surface in UHV in the STM chamber to study the influence of light on these surfaces.

Analytical techniques

Image processing of STM data was conducted using Gwyddion software,[98] ensuring precise measurements and interpret-

ations. Atomic structural models of molecular structures and 3AGNRs were generated and optimized using ChemDraw software.[99]

Author contributions

M. R.: experiments, data analysis, writing, review and editing, scientific discussion, model drawing. B. Y: writing, review and editing, scientific discussion. X. M., S. Y.: assistance in experiments, scientific discussion. J. Z., M. Z. and X. C.: assistance in experiments. H. Z.: scientific discussion. F. A.: review and editing, scientific discussion. B. W.: review, editing, scientific discussion. L. C.: review and editing, scientific discussion, supervision. J. V. B.: review and editing, scientific discussion, supervision.

Data availability

The data are available within the article and its ESI.† Raw data sets used are available from the authors upon reasonable request.

Conflicts of interest

There are no conflicts to declare.

Acknowledgements

References

1 M. Fritton, D. A. Duncan, P. S. Deimel, A. Rastgoo-Lahrood, F. Allegretti, J. V. Barth, W. M. Heckl, J. Björk and M. Lackinger, *J. Am. Chem. Soc.*, 2019, **141**, 4824–4832.

2 M. Lackinger, *Chem. Commun.*, 2017, **53**, 7872–7885.

3 M. Abadia, I. Piquero-Zulaica, J. Brede, A. Verdini, L. Floreano, J. V. Barth, J. Lobo-Checa, M. Corso and C. Rogero, *arXiv preprint arXiv*:2306.11388, 2023.

4 M. Abadia, I. Piquero-Zulaica, J. Brede, A. Verdini, L. Floreano, J. V. Barth, J. Lobo-Checa, M. Corso and C. Rogero, *Nano Lett.*, 2024, **24**, 1923–1930.

5 H. Zhang, H. Lin, K. Sun, L. Chen, Y. Zagranyarski, N. Aghdassi, S. Duhm, Q. Li, D. Zhong and Y. Li, *J. Am. Chem. Soc.*, 2015, **137**, 4022–4025.

6 F. Ullmann and J. Bielecki, *Ber. Dtsch. Chem. Ges.*, 1901, **34**, 2174–2185.

7 L. Lafferentz, V. Eberhardt, C. Dri, C. Africh, G. Comelli, F. Esch, S. Hecht and L. Grill, *Nat. Chem.*, 2012, **4**, 215–220.

8 Y.-Q. Zhang, T. Paintner, R. Hellwig, F. Haag, F. Allegretti, P. Feulner, S. Klyatskaya, M. Ruben, A. P. Seitsonen and J. V. Barth, *J. Am. Chem. Soc.*, 2019, **141**, 5087–5091.

9 C. M. Doyle, C. McGuinness, A. P. Lawless, A. B. Preobrajenski, N. A. Vinogradov and A. A. Cafolla, *Phys. Status Solidi B*, 2019, **256**, 1800349.

10 L. Grill, M. Dyer, L. Lafferentz, M. Persson, M. V. Peters and S. Hecht, *Nat. Nanotechnol.*, 2007, **2**, 687–691.

11 M. Bieri, M.-T. Nguyen, O. Gröning, J. Cai, M. Treier, K. Ait-Mansour, P. Ruffieux, C. A. Pignedoli, D. Passerone and M. Kastler, *J. Am. Chem. Soc.*, 2010, **132**, 16669–16676.

12 V. Langlais, K. Schneider and H. Tang, *J. Phys.: Condens. Matter*, 2021, **34**, 055001.

13 K. Sun, X. Li, L. Chen, H. Zhang and L. Chi, *J. Phys. Chem. C*, 2020, **124**, 11422–11427.

14 P. Ruffieux, S. Wang, B. Yang, C. Sánchez-Sánchez, J. Liu, T. Dienel, L. Talirz, P. Shinde, C. A. Pignedoli and D. Passerone, *Nature*, 2016, **531**, 489–492.

15 X. Zhou, F. Bebensee, Q. Shen, R. Bebensee, F. Cheng, Y. He, H. Su, W. Chen, G. Q. Xu and F. Besenbacher, *Mater. Chem. Front.*, 2017, **1**, 119–127.

16 K. Sun, P. Ji, J. Zhang, J. Wang, X. Li, X. Xu, H. Zhang and L. Chi, *Small*, 2019, **15**, 1804526.

17 S. Wang, W. Wang and N. Lin, *Phys. Rev. Lett.*, 2011, **106**, 206803.

18 V. V. Ivanovskaya, A. Zobelli, A. Basagni, S. Casalini, L. Colazzo, F. de Boni, D. G. de Oteyza, M. Sambi and F. Sedona, *J. Phys. Chem. C*, 2022, **127**, 393–402.

19 S. Jiang, T. Neuman, A. Boeglin, F. Scheurer and G. Schull, *Science*, 2023, **379**, 1049–1054.

20 X. Ma, Y. Shi, J. Liu, X. Li, X. Cui, S. Tan, J. Zhao and B. Wang, *J. Am. Chem. Soc.*, 2022, **144**, 13565–13573.

21 D. Guo, P. Guo, S. Tan, M. Feng, L. Cao, Z.-X. Liu, K. Liu, Z.-Y. Lu and W. Ji, *Sci. Bull.*, 2022, **67**, 1954.

22 U. Bhanu, M. R. Islam, L. Tetard and S. I. Khondaker, *Sci. Rep.*, 2014, **4**, 5575.

23 N. Lin, S. Stepanow, M. Ruben and J. V. Barth, *Templates in Chemistry III*, 2009, pp. 1–44.

24 S. Clair and D. G. de Oteyza, *Chem. Rev.*, 2019, **119**, 4717–4776.

25 L. Grill and S. Hecht, *Nat. Chem.*, 2020, **12**, 115–130.

26 J. V. Barth, *Annu. Rev. Phys. Chem.*, 2007, **58**, 375–407.

27 F. Kraushofer, Z. Jakub, M. Bichler, J. Hulva, P. Drmota, M. Weinold, M. Schmid, M. Setvin, U. Diebold and P. Blaha, *J. Phys. Chem. C*, 2018, **122**, 1657–1669.

28 M. Uphoff, *Atomistic Investigations and Control of Novel Quantum Materials: Lanthanide-Organic Nano-Architectures at Well-Defined substrates and the Iron Silicide (110) Facet*, Technische Universität München, 2019.

29 H. Zheng, J. Kröger and R. Berndt, *Phys. Rev. Lett.*, 2012, **108**, 076801.

30 A. Gloystein and N. Nilius, *Phys. Status Solidi B*, 2021, **258**, 2100337.

31 Y. Li, H. Chen, W. Wang, W. Huang, Y. Ning, Q. Liu, Y. Cui, Y. Han, Z. Liu and F. Yang, *Nano Res.*, 2020, **13**, 1677–1685.

32 J. Li, S. Wieghold, M. A. Öner, P. Simon, M. V. Hauf, E. Margapoti, J. A. Garrido, F. Esch, C.-A. Palma and J. V. Barth, *Nano Lett.*, 2014, **14**, 4486–4492.

33 A. J. Mayne and G. Dujardin, *New Diamond Front. Carbon Technol.*, 2005, **15**, 265–274.

34 C. A. Walenta, S. L. Kollmannsberger, R. N. Pereira, M. Tschurl, M. Stutzmann and U. Heiz, *J. Phys. Chem. C*, 2017, **121**, 16393–16398.

35 J. Repp, G. Meyer, F. E. Olsson and M. Persson, *Science*, 2004, **305**, 493–495.

36 M. Hollerer, D. Lüftner, P. Hurdax, T. Ules, S. Soubatch, F. S. Tautz, G. Koller, P. Puschnig, M. Sterrer and M. G. Ramsey, *ACS Nano*, 2017, **11**, 6252–6260.

37 M. Pörtner, Y. Wei, A. Riss, K. Seufert, M. Garnica, J. V. Barth, A. P. Seitsonen, L. Diekhöner and W. Auwärter, *Adv. Mater. Interfaces*, 2020, **7**, 2000080.

38 S. Wieghold, J. Li, P. Simon, M. Krause, Y. Avlasevich, C. Li, J. A. Garrido, U. Heiz, P. Samorì and K. Müllen, *Nat. Commun.*, 2016, **7**, 10700.

39 M. Kolmer, R. Zuzak, A. A. A. Zebari, S. Godlewski, J. S. Prauzner-Bechcicki, W. Piskorz, F. Zasada, Z. Sojka, D. Bléger and S. Hecht, *Chem. Commun.*, 2015, **51**, 11276–11279.

40 U. Diebold, *Surf. Sci. Rep.*, 2003, **48**, 53–229.

41 M. Kolmer, A.-K. Steiner, I. Izydorczyk, W. Ko, M. Engelund, M. Szymonski, A.-P. Li and K. Amsharov, *Science*, 2020, **369**, 571–575.

42 A. C. Papageorgiou, *Surface Studies of Titania Related Nanostructures*, University of London, 2007.

43 A. C. Papageorgiou, C. L. Pang, Q. Chen and G. Thornton, *ACS Nano*, 2007, **1**, 409–414.

44 G. Vasseur, M. Abadia, L. A. Miccio, J. Brede, A. Garcia-Lekue, D. G. de Oteyza, C. Rogero, J. Lobo-Checa and J. E. Ortega, *J. Am. Chem. Soc.*, 2016, **138**, 5685–5692.

45 R. Bennett, S. Poulston, P. Stone and M. Bowker, *Phys. Rev. B: Condens. Matter Mater. Phys.*, 1999, **59**, 10341.

46 G. S. Rohrer, V. E. Henrich and D. A. Bonnell, *Science*, 1990, **250**, 1239–1241.

47 S. Tan, H. Feng, Q. Zheng, X. Cui, J. Zhao, Y. Luo, J. Yang, B. Wang and J. Hou, *J. Am. Chem. Soc.*, 2019, **142**, 826–834.

48 W. Chu, S. Tan, Q. Zheng, W. Fang, Y. Feng, O. V. Prezhdo, B. Wang, X.-Z. Li and J. Zhao, *Sci. Adv.*, 2022, **8**, eabo2675.

49 D. A. Dankovic and E. D. Kuempel, *Occupational Exposure to Titanium Dioxide*, 2011.

50 G. Herman and Y. Gao, *Thin Solid Films*, 2001, **397**, 157–161.

51 Y. Liang, S. Gan, S. A. Chambers and E. I. Altman, *Phys. Rev. B: Condens. Matter Mater. Phys.*, 2001, **63**, 235402.

52 R. Tanner, Y. Liang and E. Altman, *Surf. Sci.*, 2002, **506**, 251–271.

53 M. Setvín, U. Aschauer, P. Scheiber, Y.-F. Li, W. Hou, M. Schmid, A. Selloni and U. Diebold, *Science*, 2013, **341**, 988–991.

54 M. Setvin, J. Hulva, G. S. Parkinson, M. Schmid and U. Diebold, *Proc. Natl. Acad. Sci. U. S. A.*, 2017, **114**, E2556–E2562.

55 Y. Mao, X. Ma, D. Wu, C. Lin, H. Shan, X. Wu, J. Zhao, A. Zhao and B. Wang, *Nano Lett.*, 2020, **20**, 8067–8073.

56 X. Ma, Z. Cheng, M. Tian, X. Liu, X. Cui, Y. Huang, S. Tan, J. Yang and B. Wang, *Nano Lett.*, 2020, **21**, 430–436.

57 A. L. Linsebigler, G. Lu and J. T. Yates Jr., *Chem. Rev.*, 1995, **95**, 735–758.

58 P. Scheiber, M. Fidler, O. Dulub, M. Schmid, U. Diebold, W. Hou, U. Aschauer and A. Selloni, *Phys. Rev. Lett.*, 2012, **109**, 136103.

59 R. Waser and M. Aono, *Nat. Mater.*, 2007, **6**, 833–840.

60 J. Suntivich, H. A. Gasteiger, N. Yabuuchi, H. Nakanishi, J. B. Goodenough and Y. Shao-Horn, *Nat. Chem.*, 2011, **3**, 546–550.

61 Y. He, O. Dulub, H. Cheng, A. Selloni and U. Diebold, *Phys. Rev. Lett.*, 2009, **102**, 106105.

62 M. Lackinger, *Trends Chem.*, 2022, **4**, 471–474.

63 Y. He, H. Jiang, S. Yuan, J. Lu and Q. Sun, *Chin. Chem. Lett.*, 2024, **35**, 109807.

64 M. Lackinger, *Dalton Trans.*, 2021, **50**, 10020–10027.

65 M. Zimmermann, D. Domke and M. Schween, *World J. Chem. Educ.*, 2021, **9**, 175–184.

66 H. Katayanagi, N. Yonekuira and T. Suzuki, *Chem. Phys.*, 1998, **231**, 345–353.

67 F. Zhang, W.-J. Ding and W.-H. Fang, *J. Chem. Phys.*, 2006, **125**, 184305.

68 S.-h. Dong, A.-l. Wang, J. Zhao, S.-j. Tan and B. Wang, *ChJCP*, 2020, **33**, 349–356.

69 X. Cui, B. Wang, Z. Wang, T. Huang, Y. Zhao, J. Yang and J. Hou, *J. Chem. Phys.*, 2008, **129**, 044703.

70 Z. Wang, R. Yin, Z. Tang, H. Du, Y. Liang, X. Wang, Q.-S. Deng, Y.-Z. Tan, Y. Zhang and C. Ma, *Phys. Rev. Lett.*, 2024, **133**, 036401.

71 R. Yin, J. Wang, Z.-L. Qiu, J. Meng, H. Xu, Z. Wang, Y. Liang, X.-J. Zhao, C. Ma and Y.-Z. Tan, *J. Am. Chem. Soc.*, 2022, **144**, 14798–14808.

72 F. Haag, Master, Technische Universität München, 2017.

73 P. J. Møller and M.-C. Wu, *Surf. Sci.*, 1989, **224**, 265–276.

74 H. Onishi and Y. Iwasawa, *Surf. Sci.*, 1994, **313**, L783–L789.

75 M. Sander and T. Engel, *Surf. Sci.*, 1994, **302**, L263–L268.

76 Q. Guo, I. Cocks and E. Williams, *Phys. Rev. Lett.*, 1996, **77**, 3851.

77 A. Berkó and F. Solymosi, *Langmuir*, 1996, **12**, 1257–1261.

78 S. Halpegamage, L. Bignardi, P. Lacovig, A. Kramer, Z.-H. Wen, X.-Q. Gong, S. Lizzit and M. Batzill, *J. Phys. Chem. C*, 2016, **120**, 26414–26424.

79 A. Rønnau, *A Closer Look at the TiO₂ (110) Surface with STM*, University of Aarhus, Denmark, 2003.

80 M. Miyazaki, Y. Sugawara and Y. J. Li, *Langmuir*, 2021, **37**, 10588–10593.

81 J. Langevoort, I. Sutherland, L. Hanekamp and P. Gellings, *Appl. Surf. Sci.*, 1987, **28**, 167–179.

82 B. J. Tan, K. J. Klabunde and P. M. Sherwood, *Chem. Mater.*, 1990, **2**, 186–191.

83 Y. I. Kim and W. E. Hatfield, *Inorg. Chim. Acta*, 1991, **188**, 15–24.

84 J. Carver, G. Schweitzer and T. A. Carlson, *J. Chem. Phys.*, 1972, **57**, 973–982.

85 I. Shabanova and V. Trapeznikov, *J. Electron Spectrosc. Relat. Phenom.*, 1975, **6**, 297–307.

86 M. Barber, J. Connor, L. Derrick, M. Hall and I. Hillier, *J. Chem. Soc., Faraday Trans. 2*, 1973, **69**, 559–562.

87 A. B. Fischer, M. S. Wrighton, M. Umana and R. W. Murray, *J. Am. Chem. Soc.*, 1979, **101**, 3442–3446.

88 S. L. T. Andersson and R. F. Howe, *J. Phys. Chem.*, 1989, **93**, 4913–4920.

89 C. M. Yim, C. L. Pang and G. Thornton, *Surf. Sci.*, 2016, **650**, 71–75.

90 J. Abad, C. Gonzalez, P. De Andres and E. Roman, *Phys. Rev. B: Condens. Matter Mater. Phys.*, 2010, **82**, 165420.

91 Y. Ohashi, N. Nagatsuka, S. Ogura and K. Fukutani, *J. Phys. Chem. C*, 2019, **123**, 10319–10324.

92 K. Schierbaum, S. Fischer, M. Torquemada, J. De Segovia, E. Roman and J. Martin-Gago, *Surf. Sci.*, 1996, **345**, 261–273.

93 Y. Chung, W. Lo and G. Somorjai, *Surf. Sci.*, 1977, **64**, 588–602.

94 A. Basagni, G. Vasseur, C. A. Pignedoli, M. Vilas-Varela, D. Peña, L. Nicolas, L. Vitali, J. Lobo-Checa, D. G. De Oteyza and F. Sedona, *ACS Nano*, 2016, **10**, 2644–2651.

95 N. Merino-Díez, A. Garcia-Lekue, E. Carbonell-Sanromà, J. Li, M. Corso, L. Colazzo, F. Sedona, D. Sánchez-Portal, J. I. Pascual and D. G. de Oteyza, *ACS Nano*, 2017, **11**, 11661–11668.

96 N. Merino-Díez, J. Lobo-Checa, P. Nita, A. Garcia-Lekue, A. Basagni, G. Vasseur, F. Tiso, F. Sedona, P. K. Das and J. Fujii, *J. Phys. Chem. Lett.*, 2018, **9**, 2510–2517.

97 G. Vasseur, Y. Fagot-Revurat, M. Sicot, B. Kierren, L. Moreau, D. Malterre, L. Cardenas, G. Galeotti, J. Lipton-Duffin and F. Rosei, *Nat. Commun.*, 2016, **7**, 10235.

98 D. Nečas and P. Klapetek, *Open Phys.*, 2012, **10**, 181–188.

99 Z. Li, H. Wan, Y. Shi and P. Ouyang, *J. Chem. Inf. Comput. Sci.*, 2004, **44**, 1886–1890.